Title

Coseismic Rupture Process of the Large 2019 Ridgecrest Earthquakes From Joint Inversion of Geodetic and Seismological Observations

Journal

Geophysical Research Letters, 46(21)

ISSN

0094-8276

Authors

Liu, Chengli
Lay, Thorne
Brodsky, Emily E
et al.

Publication Date

2019-11-16

DOI

10.1029/2019gl084949

Peer reviewed

Geophysical Research Letters

RESEARCH LETTER
10.1029/2019GL084949

Coseismic Rupture Process of the Large 2019 Ridgecrest Earthquakes From Joint Inversion of Geodetic and Seismological Observations

Chengli Liu[1,2], Thorne Lay[2], Emily E. Brodsky[2], Kelian Dascher-Cousineau[2], and Xiong Xiong[1]

[1]Hubei Subsurface Multi-Scale Imaging Key Laboratory, Institute of Geophysics and Geomatics, China University of Geosciences, Wuhan, China, [2]Department of Earth and Planetary Sciences, University of California, Santa Cruz, CA, USA

Key Points:
- The 2019 Ridgecrest earthquake sequence began with rupture of orthogonal faults in a M_{WW} 6.5 earthquake, with most slip on a NE-SW fault
- A larger, M_{WW} 7.1 mainshock extended along a sequence of NW-SE strike-slip segments straddling a short segment ruptured in the foreshock
- Low rupture velocity and radiated energy with high aftershock production accompany immature fault zone rupture triggering a larger event

Supporting Information:
- Supporting Information S1
- Movie S1
- Data Set S1
- Data Set S2

Correspondence to:
T. Lay,
tlay@ucsc.edu

Citation:
Liu, C., Lay, T., Brodsky, E. E., Dascher-Cousineau, K., & Xiong, X. (2019). Coseismic rupture process of the large 2019 Ridgecrest earthquakes from joint inversion of geodetic and seismological observations. *Geophysical Research Letters*, *46*, 11,820–11,829. https://doi.org/10.1029/2019GL084949

Received 10 AUG 2019
Accepted 16 OCT 2019
Accepted article online 25 OCT 2019
Published online 6 NOV 2019

Abstract On 4 and 6 July 2019, two large strike-slip earthquakes with *W*-phase moment magnitudes M_{WW} 6.5 (foreshock) and M_{WW} 7.1 (mainshock) struck the Eastern California Shear Zone, northeast of Ridgecrest. The faulting geometry and kinematic coseismic slip distribution of both events are determined by jointly inverting seismological and geodetic observations guided by aftershock and surface rupture locations. The foreshock ruptured two orthogonal faults with a prominent L-shaped geometry with maximum slip of ~1.1 m on the NE-SW segment. The mainshock faulting extended NW-SE along several primary fault segments that straddle the foreshock slip. The surface rupture and slip model indicate mostly near-horizontal strike-slip motion with maximum slip of ~3.7 m, but there is a localized vertical dip-slip motion. Both the foreshock and mainshock ruptures terminate in regions of complex surface offsets. High aftershock productivity and low rupture velocity may be the result of rupture of a relatively immature fault system.

Plain Language Summary Two large earthquakes on 4 July 2019 (magnitude 6.5) and 6 July 2019 (magnitude 7.1) struck northeast of Ridgecrest, California. Earthquakes such as the 1995 Ridgecrest earthquake have occurred previously in this broad region, called the Eastern California Shear Zone, but the deformation is not concentrated into a dominant single fault. The first rupture involved slip on two perpendicular faults, one aligned NE-SW and the other NW-SE, with slip and aftershocks forming an L-shaped pattern. Most slip was on the NE-SW fault. The mainshock ruptured a sequence of NW-SE trending faults, with slip extending across the short NW-SE segment ruptured in the foreshock. Both ruptures were delimited by zones of multiple surface fractures. The rupture for the mainshock expanded relatively slowly with low radiated energy, and a large number of aftershocks occurred, suggesting rupture of an immature segmented fault system.

1. Introduction

The Eastern California Shear Zone (ECSZ) continues to generate large strike-slip earthquakes aligned with the Pacific-North American relative plate motion direction along a trend that extends northwestward from the southernmost San Andreas Fault. The 28 June 1992 Landers (M_W 7.3) and 16 October 1999 Hector Mine (M_W 7.1) events ruptured the southern ECSZ (Figure 1a). The region northeast of Ridgecrest in the central ECSZ recently ruptured in two large events (Figure 1b); 4 July 2019 (17:33:49.04 UTC, 35.705°N 117.504°W, 10.5 km deep, *W*-phase M_{WW} 6.5; U.S. Geological Survey-National Earthquake Information Center [USGS-NEIC]: https://earthquake.usgs.gov/earthquakes/search/) and 6 July 2019 (03:19:53.04 UTC, 35.770°N, 117.599°W, 8.0 km deep, M_{WW} 7.1; USGS-NEIC). These events extend the last few decades of occurrence of large earthquakes in southern California located either west or east of the locked portion of the San Andreas Fault from Parkfield to the Imperial Valley.

The 2019 Ridgecrest earthquakes involve predominantly strike-slip faulting, with dominant deformation along the NW-SE trend of the ECSZ; however, the 4 July 2019 foreshock had minor slip along this direction, with most slip located on an orthogonal fault strand trending NE-SW. The early aftershocks of the 4 July event defined an L-shaped distribution indicating this faulting complexity (Figure 2a). The mainshock initiated just to the northwest of the rupture zone of the foreshock, with aftershocks and surface rupture distributed on a system of NW-SE trending fault segments that straddle the foreshock rupture zone (Figure 2b). About 10% of the aftershock activity occurred in the Coso Volcanic Field to the northwest, beyond the

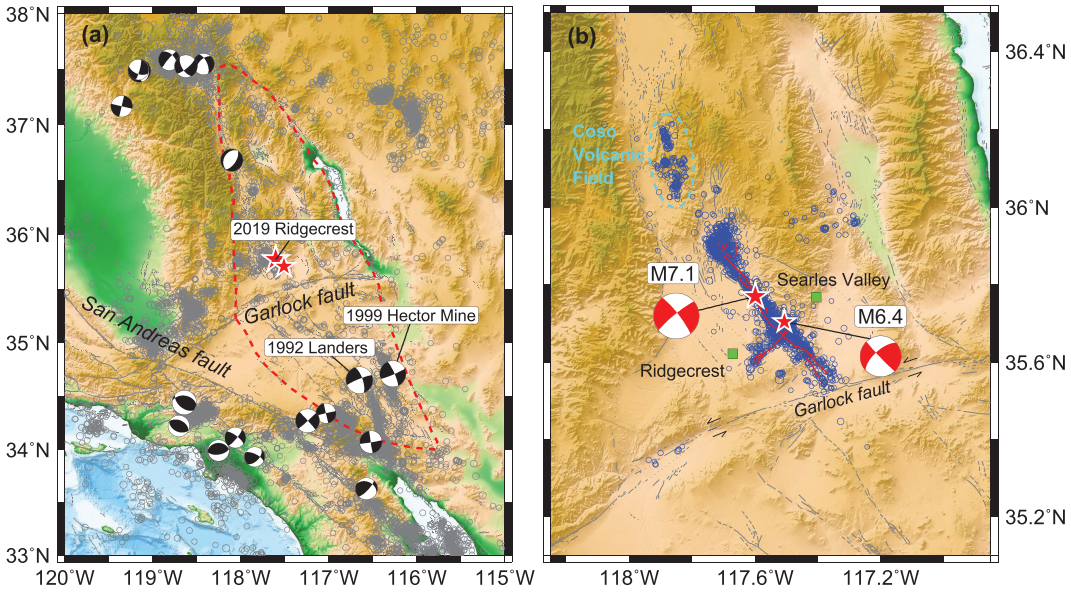

Figure 1. (a) Tectonic setting and seismicity in southern California. Gray circles with magnitude-scaled radius show earthquakes from the U.S. Geological Survey-National Earthquake Information Center with $M \geq 2.5$. Black focal mechanisms are magnitude-scaled Global Centroid Moment Tensor solutions plotted at the centroid location. Gray lines are active faults. Red stars indicate foreshock and mainshock epicenters. Red dashed line outlines the Eastern California Shear Zone. (b) Source region of the 2019 Ridgecrest earthquake sequence. Blue circles are magnitude-scaled 1-month aftershocks from U.S. Geological Survey-National Earthquake Information Center with $M \geq 2.5$. Red stars and focal mechanisms are epicenters and Global Centroid Moment Tensor solutions for the foreshock and mainshock, respectively. The Coso Volcanic Field is highlighted in cyan. Green squares indicate Ridgecrest and Searles Valley town locations. Gray lines are active faults.

rupture zone, and rupture extended southeastward to within ~10 km of the ENE trending Garlock fault. Prior activity in the source region includes the 1995 Ridgecrest M_L 5.4 and 5.8 earthquakes (e.g., Hauksson et al., 1995), the larger of which had strike-slip faulting along an NW-SE trend located a few kilometers westward from the 2019 mainshock rupture zone. Earthquake swarms in 1980–1981 and prior moderate earthquakes with magnitudes from 5.0 to 6.3 have occurred tens of kilometers to the west of the Ridgecrest sequences during the last century and numerous faults (USGS: https://earthquake.usgs.gov/data/data.php#earth) with predominantly northward trends that have been mapped in the region, but there was no well-defined NW-SE fault mapped in the vicinity of the rupture, consistent with what would be expected for an immature fault system.

The rupture characteristics of the foreshock and mainshock are herein established using seismic and geodetic observations with constraints from the aftershock distributions and mapped surface ruptures. The rupture kinematics and aftershock sequence are then considered in the context of an immature fault system, evolving on the margins of the seismogenic halo around the locked central San Andreas Fault.

2. Data Processing and Faulting Geometry

Numerous seismic and GPS stations recorded the coseismic ground motions produced by the large events in the 2019 Ridgecrest earthquake sequence. For the foreshock, we select strong motion recordings from 40 stations with epicentral distances ≤150 km (Figure 2a and Figure S1 in the supporting information) to minimize scattering effects accumulated over longer propagation distances. All strong motion waveforms are accessed from the Center for Engineering Strong Motion Data. We remove baseline drift following Wang et al. (2011), integrate the accelerations to velocity, and band-pass filter all recordings in the frequency band 0.02 to 0.5 Hz. We assign the closest stations (red triangles in Figure S1) twice the weight in the inversion (discussed below), because near-fault recordings have more sensitivity to the slip model details than more distant data. We select coseismic GPS static displacements at 41 sites available from the University NAVigation System using Timing And Ranging Consortium (UNAVCO; Figures 2a and S2). Due to their larger uncertainties, all vertical components are downweighted by a factor of 0.5 in the joint inversion.

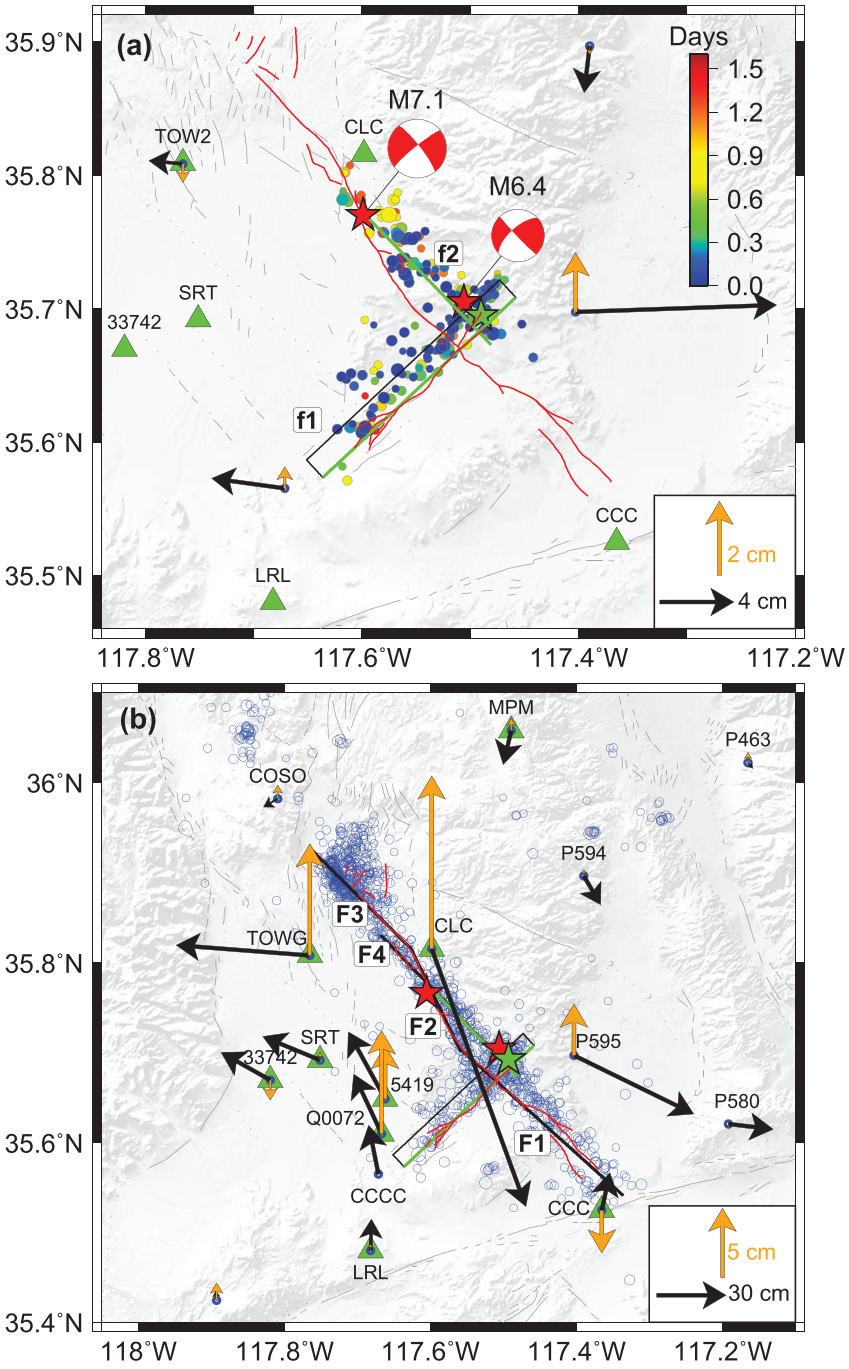

Figure 2. (a) Map of the foreshock fault geometry and aftershocks (circles, color coded by lag time). Green lines represent fault segments. (b) Map of the mainshock fault geometry and 1-month aftershocks (blue circles). Green triangles indicate nearby strong motion station locations, all stations used are shown in Figures S1 and S3. Nearby subsets of coseismic static horizontal and vertical displacements are displayed in black and orange arrows, respectively. All static displacement observations used are indicated in Figures S2 and S4. Black lines indicate fault segments. Red stars indicate foreshock and mainshock epicenter locations; the green star indicates the perturbed epicenter of the foreshock for the joint finite-fault inversion. Red lines represent surface ruptures mapped by the U.S. Geological Survey, and gray lines indicate regional faults.

Guided by early summaries of surface rupture and/or decorrelation lineations (USGS: https://www.usgs.gov/media/images/surface-ruptures-july-4-and-5-ridgecrest-ca-earthquakes; National Aeronautics and Space Administration: https://disasters.nasa.gov/southern-california-earthquakes-july-2019/) and the initial

catalog aftershock distribution (Figure 2a), we conduct a series of preliminary finite fault inversions to explore constraints on the fault geometry (see the supporting information). Ultimately, we adopt a model with two perpendicular fault segments with an L-shaped pattern, labeled f1 and f2, with strikes of 227° and 316°, respectively (Table S1). The rupture initiates on segment f1, which has a dip of 85°. This dip was adopted based on the series of preliminary finite-fault inversions of the strong motion data and is compatible with the 73° to 90° range of teleseismic long-period point source fault orientations (Global Centroid Moment Tensor [GCMT], https://www.globalcmt.org/CMTsearch.html, and USGS-NEIC, https://earthquake.usgs.gov/earthquakes/search/) and the initial California Integrated Seismic Network aftershock locations. Segment f2 has a dip of 90°.

For the mainshock, we select strong motion recordings from 63 stations with epicentral distances ≤200 km (Figures 2b and S3). The drift-corrected accelerograms are integrated to obtain ground velocity and then band-pass filtered between 0.02 and 0.5 Hz. This data set was subdivided into three epicentral distance groups to assign weights: Group 1 (nine close-in stations) has weights of four (red triangles in Figure S3), Group 2 (22 intermediate-distance stations) has weights of two (green triangles in Figure S3), and Group 3 (32 large-distance stations) has weights of one, (blue triangles in Figure S3).

The mainshock coseismic GPS static displacements (UNAVCO) at 329 sites are selected for the joint inversion (Figures 2b and S4). Considering their associated absolute errors, we assign near-fault displacements (red circles in Figure S4) twice the weight of the distant displacements. We also incorporate three-component coseismic displacements derived from eight near-field strong motion stations (Table S2), for which the baseline stability is good (Figure S5). For example, the displacements computed at station TOW2 are similar to GPS displacements at TOWG (Green arrows in Figure S4). These eight stations have the same weight as near-fault GPS sites in the joint inversion.

We select 41 broadband teleseismic *P* waves and 31 *SH* waves with high signal-to-noise ratio and good azimuthal coverage (Figure S6), downloaded from the Incorporated Research Institutions for Seismology data center. Instrument responses are removed to obtain ground velocities (e.g., Wald et al., 1996), band-pass filtered with corner frequencies of 0.0033 to 1 Hz. The teleseismic *P* and *SH* first arrivals are aligned manually.

The mainshock appears to have ruptured a complex fault system, as indicated by the surface rupture traces and aftershock distribution, which extend 50 km along an NW-SE trend (Figure 1b). We again conduct a series of preliminary finite fault inversions, considering single and multiple segment models to specify the fault segment geometries (see the supporting information). Ultimately, we represent the mainshock faulting with four vertical rupture segments (Figure 2b), labeled F1, F2, F3, and F4 with strikes of 315°, 334°, 312°, and 316°, respectively (Table S1). The labeling of the segments is from south to north for F1 to F3, with F4 involving an additional segment slightly oblique to F2 and F3. The dip of the segments was set to 90° based on the initial inversions; teleseismic point source fault orientations have dips ranging from 73° to 84° (GCMT; USGS-NEIC). Segments F2 and F4 may converge at lower crustal depth but appear to be distinct near the surface based on the surface fractures and shallow aftershocks. F4 of the mainshock and f2 of the foreshock overlap in the section between the two hypocenters (Figure 2b).

3. Model Parameterization and Inversion Strategy

For the foreshock, we subdivide the two segments into 180 subfaults with lengths of 2.5 km along strike and 1.94 km along dip. We adjust the hypocenter slightly to 35.693°N, 117.493°W, 10.5 km deep to fit the surface rupture and early aftershock distribution, placing it on segment f1. The top edges of the fault segments are 0.26 km deep (we avoid surface rupture to prevent an instability in the Green's function calculations). The four mainshock fault segments (Table S1) have the same downdip extent, with the top edges 0.28 km deep. We divide the four fault segments into 363 subfaults (2.5 km along strike and 2.27 km along dip). The rupture initiates on F2 at the USGS-NEIC hypocenter (35.770°N, 117.599°W, 8 km). We perform a finite-fault joint inversion of seismological and geodetic data in the wavelet domain (e.g., Ji et al., 2002a, 2002b; Ji et al., 2003). A simulated annealing algorithm simultaneously inverts for slip amplitude, rake angle, rupture initiation time, and rise time for each subfault, searching a range of parameters (Table S3). The weights of each dataset noted above are obtained by performing inversions with varying weights, seeking to balance the waveform fitting.

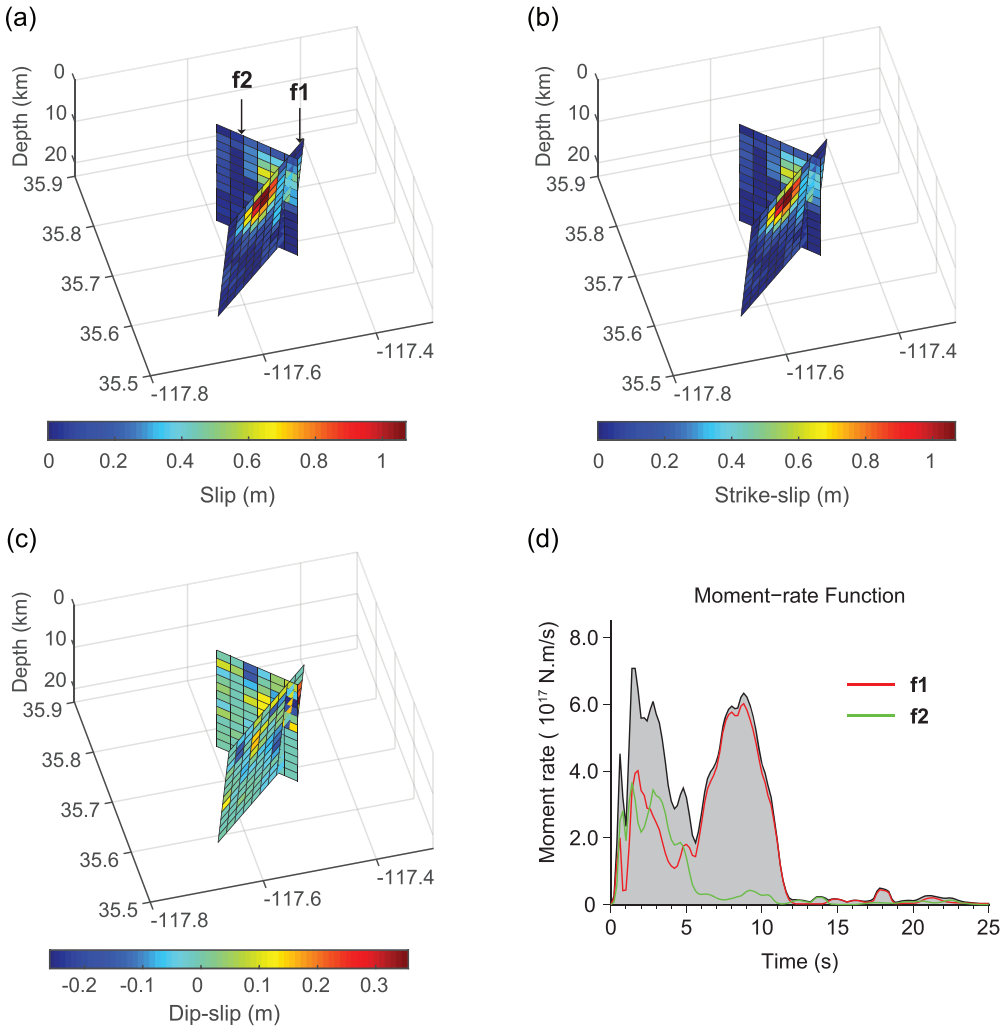

Figure 3. Three-dimensional view of the M_{WW} 6.4 foreshock slip distribution. (a) Total slip on both fault segments. (b) Strike-slip and (c) dip-slip components. Note the differences in scales. (d) Moment rate function contributions from the two fault segments and the gray-shaded total moment rate.

We assume a 1-D crustal model (Shearer et al., 2005; Figure S7) for calculating the Green's functions. Green's functions for the coseismic GPS displacements are calculated using a generalized reflection-transmission coefficient matrix method developed by Xie and Yao (1989). Strong motion Green's functions are generated using a frequency-wave number integration method (e.g., Zhu & Rivera, 2002). The teleseismic Green's functions are computed by generalized ray theory (e.g., Helmberger, 1974).

4. Rupture Inversion Results

Figure 3 shows a 3-D map view of the preferred foreshock slip distribution. The detailed slip and rise time distributions for a single fault model (Figure S8) and the preferred two-fault model (Figure S9) have similar slip on f1, with modest slip on f2 for the two-fault model. The corresponding fits to GPS static displacements and strong motion waveforms are shown in Figures S10–S12. The two-fault model matches the GPS static displacements and strong motion waveforms slightly, but systematically, better than the single fault model (Figures S10 and S11). Synthetic waveform decompositions of the contribution from the two fault segments indicate how the improved waveform fits are achieved (Figure S11c). The direction and magnitude of static displacements are very well matched, but large waveform mismatches can be seen for several near-fault strong motion stations (for example, TOW2 and SRT), particularly in the later portion of waveforms.

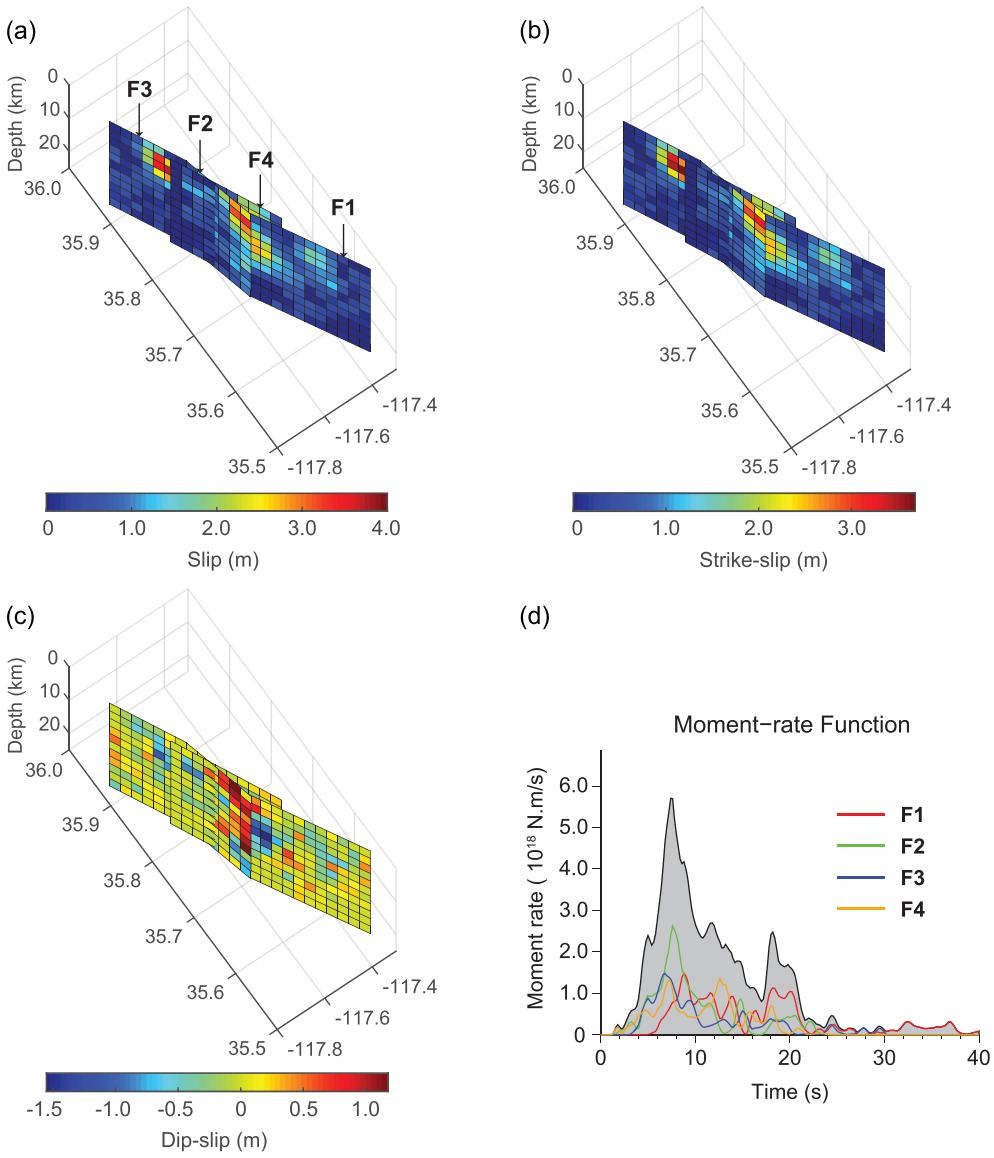

Figure 4. Three-dimensional view of the M_{WW} 7.1 mainshock slip distribution. (a) Total slip on the four fault segments. (b) Strike-slip and (c) dip-slip components. Note the differences in scales. (d) Moment rate function contributions from the four fault segments and the gray-shaded total moment rate.

These misfits, observed for both large events, are presumably due to localized 3-D basin effects not modeled using a 1-D crustal velocity model.

In our preferred joint inversion rupture model (Figures 3 and S9), the foreshock ruptured the two perpendicular faults almost simultaneously near the intersection of f1 and f2, and the moment rate function quickly reaches its first peak at about 3 s. Half of the moment released within the first 6 s of rupture and peak slip on f2 of about ~0.5 m is reached. After that, the rupture propagated to shallow depth along f1, along which there are clear surface breaks. The maximum slip on f1 is about 1.1 m of predominately strike-slip displacement (Figure 3b), corresponding to the second peak of the moment rate. Rise times are estimated to be ~1 s during the initial phase of the rupture (Figure S9) and ~4 s for the large-slip later rupture stage. The overall average rupture velocity is about 1.5 km/s, a rather low value given that the inversion allowed a range from 0.5 to 3.5 km/s (Table S3). The total seismic moment (M_0) is 5.05×10^{18} N·m (M_W 6.4). Detailed information for each fault segment is given in Table S4.

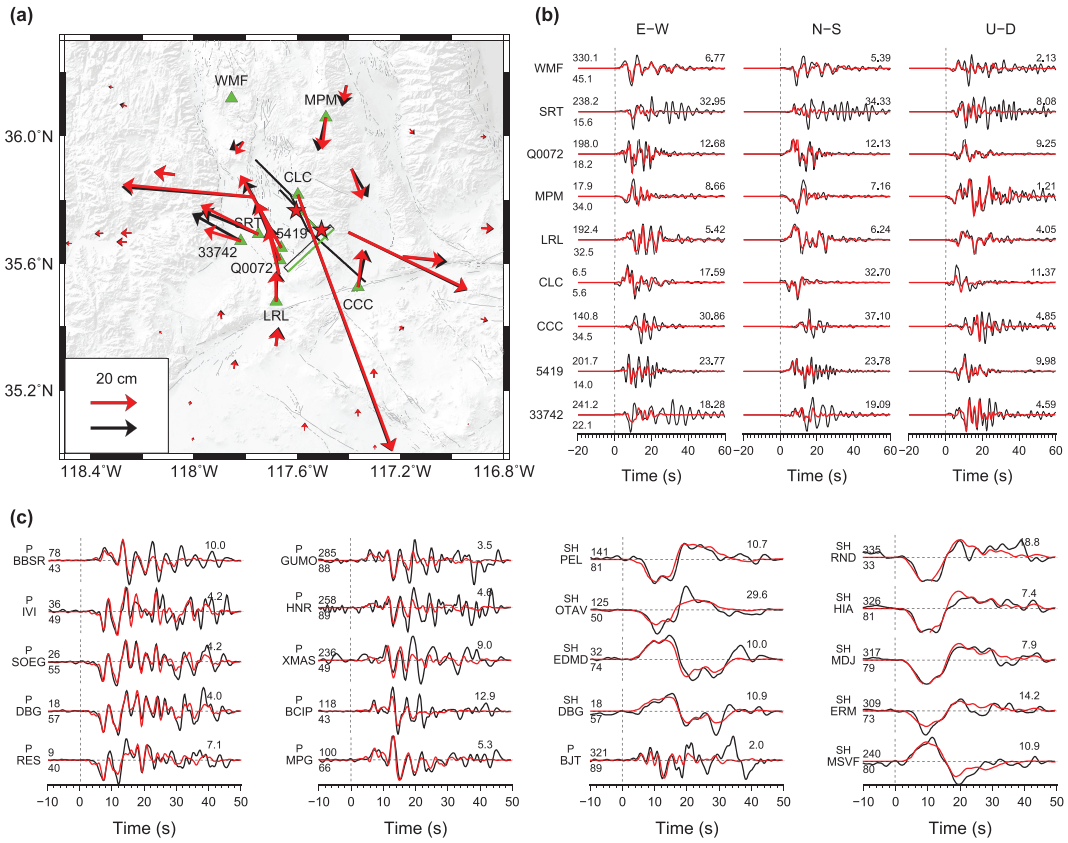

Figure 5. Comparison of subsets of the observed data and synthetics for the mainshock. (a) Coseismic horizontal static GPS displacements. (b) Strong motion velocity and (c) teleseismic velocity comparisons. Azimuth and epicentral distance for each station are indicated above and below the waveform leader, respectively. The number at the end of each record is the peak value of the observed data in micrometers per second (teleseismic data) or in centimeters per second (strong motion data). Comparisons of all data and synthetics are shown in Figures S19 to S21.

We favor a four-segment model for the mainshock rupture over models with one segment (Figure S13) or three segments (Figure S14). Figure 4 shows a 3-D view of the preferred fault model geometry and slip distribution obtained by joint inversion. Details of the slip distributions and rise times are shown in Figure S15. The static displacement and seismic waveform fits of all datasets are shown in Figures 5 and S16–S21. Figures S16 to S18 compare subsets of strong motion and teleseismic waveform fits for three models with a different number of fault segments, showing systematic reduction in misfit for the preferred model. Figure 5 demonstrates that the four-segment model can account for the near-field observations well, and teleseismic data are satisfactorily modeled, except for some secondary features after 30 s. Near-fault strong motion data are generally matched in phase, but the amplitude at several stations is underestimated (notably, stations 33742, 5419, and SRT), which may be associated with local sediment amplification effects. Overall, uncertainties associated with the complex parameterization such as precise timing between segments and trade-offs of slip on overlapping strands are unavoidable, but the joint inversion with a four-segment fault system provides a viable representation of the complex source given the quality of the data predictions.

The mainshock rupture propagated bilaterally along the strike direction and is dominated by strike slip displacement (Figure 4b). Most slip is located near the hypocenter and extends from 0 to 20 km in depth. Four regions with large-amplitude slip are apparent (Figure S15): First one is near the intersection of F1 and F2 at depths between 0 and 20 km, which produced significant dip-slip surface rupture (Figure 4c); the second is northwest of the hypocenter on F3 at depths between 0 and 12 km, with maximum slip of 3.7 m, in a region with minor surface rupture; the third is located in the middle-upper portion of F1, with peak slip of 1 m; and the fourth occurred on F4, overlapping with f2 of the foreshock, with a maximum surface rupture of 2 m.

The rupture initiates almost simultaneously on F2 and F4 with slow rupture velocity of <1 km/s and then propagates bilaterally with average rupture velocities of 1.0–1.5 km/s. Again, these low average values are found despite allowing a range of 0.5 to 3.5 km/s (Table S3). There is a little slip on F4 north of the intersection with F2; if this half of the segment is removed, slip on F2 increases proportionately. Rupture of F1 appears to involve two separate asperities. In the northwestern segment F3 with the largest slip, rupture stopped abruptly after 10 s. Rise time variations show consistent patterns of shorter rise times at larger depth and longer at shallower depth (Figure S15) with the mean rise time over the entire rupture being ~4 s. Larger slip is found for the longer rise time regions. The entire coseismic process lasted ~40 s (Figure 4d) but over 90% of the faulting occurred within the first 25 s. The late moment release involves minor slip on F1, which is not spatially well resolved and may be an artifact. $M_0 = 5.0 \times 10^{19}$ N·m (*Mw* 7.07). More detailed information for each fault segment is given in Table S4. Movie S1 provides an animated 3-D display of the coseismic slip for the foreshock and mainshock.

5. Discussion and Conclusions

A conspicuous feature of the 2019 Ridgecrest sequence is the mutually perpendicular strike-slip faults. The kinematic inversion and the aftershock distribution both indicate that the foreshock ruptured orthogonal faults. Such faulting is viable but unexpected in conventional fault mechanics that predict ~60° angle between optimally oriented strike-slip conjugate faults (e.g., Jaeger & Cook, 1979). Mutually perpendicular conjugate faults have been observed in regions of distributed strike-slip faulting with young faults that have modest cumulative offset and low slip rate, including central Honshu, Japan, and the Salton trough (e.g., Fukuyama, 2015; Hanks & Allen, 1989; Thatcher & Hill, 1991). These fault systems have sometimes ruptured in discrete events on orthogonal ruptures, as is the case for the 1987 Superstition Hills, California M_W 6.2 and 6.5 earthquakes (e.g., Thatcher & Hill, 1991). Near-orthogonal strike-slip faulting during single earthquakes occurred in the 17 December 1987 East Chiba, Japan, earthquake (M_W 6.7; e.g., Fukuyama, 1991); the 28 June 1992 Big Bear earthquake (M_W 6.5; e.g., Jones & Hough, 1995); and the much larger 11 April 2012 Indian Ocean (M_W 8.7; e.g., Meng et al., 2012; Yue et al., 2012; Wei et al., 2013; Hill et al., 2015) and 2018 Gulf of Alaska (M_W 7.9; e.g., Ruppert et al., 2018; Lay et al., 2018; Wen et al., 2019; Zhao et al., 2019) intraplate oceanic events. The multisegment structure of the mainshock also has similarity to portions of the very complex 2016 Kaikoura, New Zealand (M_W 7.8), rupture (e.g., Hamling et al., 2017; Wang et al., 2018), which had overlapping fault segments fail collectively. We speculate that immature fault systems may be particularly prone to complex faulting in general and perpendicular strike-slip faulting in particular as a result of stress concentrations at the ends of short fault segments with rotations and cross faults between strands.

The far-field broadband radiated elastic energy is estimated as $E_r = 5.4 \times 10^{13}$ J for the foreshock and $E_r = 4.8 \times 10^{14}$ J for the mainshock (Incorporated Research Institutions for Seismology EQEnergy; https://doi.org/10.17611/DP/EQE.1), following Convers and Newman (2011). Using GCMT seismic moment estimates, $M_0 = 6.1 \times 10^{18}$ N·m (foreshock) and 4.4×10^{19} N·m (mainshock), gives moment-scaled radiated energy values, $E_r/M_0 = 0.9 \times 10^{-5}$ (foreshock) and 1.1×10^{-5} (mainshock). These are similar to the average value for large interplate thrust events (e.g., Ye et al., 2016) and lower than typical values (~4.0×10^{-5}) for large strike-slip events (e.g., Ye et al., 2015). Measurements of m_B for periods of ~3.5 s (Kanamori & Ross, 2018) are 6.08 (foreshock) and 6.71 (mainshock), predicting relatively low values of scaled radiated energy; $E_{R\_B}/M_0 = 0.5 \times 10^{-5}$ (foreshock) and 1.4×10^{-5} (mainshock; H. Kanamori, personal communication, 2 August 2019).

The relatively low radiated energy correlates with low average rupture velocity (<1.5 km/s) for the two events. While also multisegment ruptures, the 1992 Landers and 1999 Hector Mine earthquakes had higher rupture velocities (Table S5). Low rupture velocity may indicate high fracture energy and/or longer slip-weakening distance (e.g., Guatteri & Spudich, 2000).

The mainshock rupture zone is delimited by an N-S shear zone and the Coso Volcanic Field to the northwest and the Garlock fault to the southeast (Figure 1b). These geologic features form natural boundaries to the segment. There are similarities to the 2016 Kumamoto, Japan, earthquake sequence, which also had complex faulting bounded by natural boundaries (e.g., Asano & Iwata, 2016; Yagi et al., 2016). Concentrations of slip near segment boundaries for both the foreshock and the mainshock and the low rupture velocity suggest influence of the fault complexity on the rupture dynamics. The southwestern end of the foreshock rupture

has multiple surface rupture branches (Figure 2a), as do the southeastern and northwestern ends of the mainshock rupture (Figure 2b), where there is also splaying of the aftershock distribution (Figure 1b, ~50% of aftershocks locate in the northwest).

Two additional major features of the Ridgecrest earthquake are its unusually high aftershock productivity and the close spatial proximity of the large foreshock and mainshock. These aspects are likely related, as abundant aftershocks increase the likelihood that one aftershock will be large enough to define a new mainshock (e.g., Ogata, 1988). We compare aftershock productivity in 34-hr-long time windows following the foreshock and mainshock and in a 28-day-long window after the mainshock, to productivity in comparable time windows for global earthquakes using the USGS-NEIC catalog (completeness cutoff $M_c = 4.5$) and for Southern California earthquakes using the California Integrated Seismic Network catalog ($M_c = 2.5$). For instance, the aftershock productivity of the foreshock is a factor of 8.5 above the global median for the 34-hr interval, while the aftershock productivity of the mainshock is a factor of 5 above the median. Limiting the global datasets to only strike slip or only continental strike-slip subpopulations, which tend to be less productive than other faulting mechanisms, we find that the Ridgecrest events are among the most productive strike-slip earthquakes (Figure S23).

The high aftershock productivity may be linked to the rupture complexity. Multiple fault ruptures can result in a larger activated volume and hence a correspondingly high productivity (e.g., Mori, 2017). Fault complexity can also result in larger stress concentrations at fault junctions and step overs, which could also increase aftershock productivity. Since high productivity enhances statistical likelihood of triggering a subsequent mainshock, the combined implication is that complex faulting is more likely to result in a later, larger, potentially more damaging, earthquake.

The overall characteristics of the 2019 ruptures support the notion of failure of an immature fault zone involving strike-slip fault activation over an enhanced volume including orthogonal faulting, fine-scale segmentation and splaying at the ends of segments, enhanced aftershock productivity, low rupture velocity, and low radiated energy. These conditions favor an enhanced level of triggering, leading to foreshocks, and cascading faulting interactions, distinct from spontaneous nucleation of faulting on mature faults.

Acknowledgments
Teleseismic body wave waveforms were downloaded from the Incorporated Research Institutions for Seismology (IRIS) data management center (http://ds.iris.edu/wilber3/find_event). Strong motion recordings were obtained from Center for Engineering Strong Motion Data (CESMD, https://strongmotioncenter.org/). Coseismic GPS displacements were obtained from the UNAVCO Bulletin Board (https://www.unavco.org/highlights/2019/ridgecrest.html). Global Centroid Moment Tensor Solutions are from https://www.globalcmt.org/CMTsearch.html. The surface ruptures are from the USGS (https://www.usgs.gov/media/images/surface-ruptures-july-4-and-5-ridgecrest-ca-earthquakes). The USGS-NEIC catalog received contributions from the California Integrated Seismic Network (CISN), https://www.cisn.org/. Three-dimensional image figures are plotted using MATLAB. We appreciate helpful comments from H. Kanamori and thoughtful reviews from editor Gavin Hayes and two anonymous reviewers. C. Liu was supported by National Key R & D Program on Monitoring, Early Warning and Prevention of Major Natural Disaster (2017YFC1500305) and the Visiting Scholar Program of the Chinese Science Council. T. Lay's research on earthquakes is supported by U.S. National Science Foundation Grant EAR1802364. E. Brodsky is supported by U.S. National Science Foundation Grant EAR1761987.

References

Asano, K., & Iwata, T. (2016). Source rupture processes of the foreshock and mainshock in the 2016 Kumamoto earthquake sequence estimated from the kinematic waveform inversion of strong motion data. *Earth, Planets and Space*, *68*(1), 147. https://doi.org/10.1186/s40623-016-0519-9

Convers, J. A., & Newman, A. V. (2011). Global evaluation of large earthquake energy from 1997 through mid-2010. *Journal of Geophysical Research*, *116*, B08304. https://doi.org/10.1029/2010JB007928

Fukuyama, E. (1991). Inversion for the rupture details of the 1987 east Chiba earthquake, Japan, using a fault model based on the distribution of relocated aftershocks. *Journal of Geophysical Research*, *96*(B5), 8205–8217. https://doi.org/10.1029/91JB00328

Fukuyama, E. (2015). Dynamic faulting on a conjugate fault system detected by near-fault tilt measurements. *Earth, Planets and Space*, *67*(1), 38. https://doi.org/10.1186/s40623-015-0207-1

Guatteri, M., & Spudich, P. (2000). What can strong-motion data tell us about slip-weakening fault-friction laws? *Bulletin of the Seismological Society of America*, *90*(1), 98–116. https://doi.org/10.1785/0119990053

Hamling, I. J., Hreinsdóttir, S., Clark, K., Elliott, J., Liang, C., Fielding, E., et al. (2017). Complex multifault rupture during the 2016 M_W 7.8 Kaikoura earthquake, New Zealand. *Science*, *356*(6334). https://doi.org/10.1126/science.aam7194

Hanks, T. C., & Allen, C. R. (1989). The Elmore Ranch and Superstition Hills earthquakes of 24 November 1987: Introduction to the special issue. *Bulletin of the Seismological Society of America*, *79*, 231–238.

Hauksson, E., Hutton, K., Kanamori, H., Jones, L., Mori, J., Hough, S., & Roquemore, G. (1995). Preliminary report on the 1995 Ridgecrest earthquake sequence in Eastern California. *Seismological Research Letters*, *66*(6), 54–60. https://doi.org/10.1785/gssrl.66.6.54

Helmberger, D. V. (1974). Generalized ray theory for shear dislocations. *Bulletin of the Seismological Society of America*, *64*(1), 45–64.

Hill, E. M., Yue, H., Barbot, S., Lay, T., Tapponnier, P., Hermawan, I., et al. (2015). The 2012 M_W 8.6 Wharton Basin sequence: A cascade of great earthquakes generated by near-orthogonal, young, oceanic-mantle faults. *Journal of Geophysical Research: Solid Earth*, *120*, 3723–3747. https://doi.org/10.1002/2014JB011703

Jaeger, J. G., & Cook, N. G. W. (1979). *Fundamentals of rock mechanics*, (third ed.p. 585). London: Chapman and Hall.

Ji, C., Helmberger, D. V., Wald, D. J., & Ma, K. F. (2003). Slip history and dynamic implications of the 1999 Chi-Chi, Taiwan, earthquake. *Journal of Geophysical Research*, *108*(B9), 2412. https://doi.org/10.1029/2002JB001764

Ji, C., Wald, D. J., & Helmberger, D. V. (2002a). Source description of the 1999 Hector Mine, California, earthquake, Part I: Wavelet domain inversion theory and resolution analysis. *Bulletin of the Seismological Society of America*, *92*(4), 1192–1207. https://doi.org/10.1785/0120000916

Ji, C., Wald, D. J., & Helmberger, D. V. (2002b). Source description of the 1999 Hector Mine, California, earthquake, part II: Complexity of slip history. *Bulletin of the Seismological Society of America*, *92*(4), 1208–1226. https://doi.org/10.1785/0120000917

Jones, L. E., & Hough, S. E. (1995). Analysis of broadband records from the 28 June 1992 Big Bear earthquake: Evidence of a multiple-event source. *Bulletin of the Seismological Society of America*, *85*(3), 688–704.

Kanamori, H., & Ross, Z. E. (2018). Reviving m_B. *Geophysical Journal International*, *216*(3), 1798–1816. https://doi.org/10.1093/gji/ggy510

Lay, T., Ye, L., Bai, Y., Cheung, K. F., & Kanamori, H. (2018). The 2018 M_W 7.9 Gulf of Alaska earthquake: Multiple fault rupture in the Pacific plate. *Geophysical Research Letters*, *45*, 9542–9551. https://doi.org/10.1029/2018GL079813

Meng, L., Ampuero, J.-P., Stock, J., Duputel, Z., Luo, Y., & Tsai, V. C. (2012). Earthquake in a maze: Compressional rupture branching during the 2012 M_W 8.6 Sumatra earthquake. *Science*, *337*(6095), 724–726. https://doi.org/10.1126/science.1224030

Mori, J. J. (2017). Temporal characteristics of recent aftershock sequences from moderate-sized earthquakes of onshore Japan. (abstract S34B-02). American Geophysical Union Fall Meeting, https://agu.confex.com/agu/fm17/meetingapp.cgi/Paper/276087

Ogata, Y. (1988). Statistical models for earthquake occurrences and residual analysis for point processes. *Journal of the American Statistical Association*, *83*(401), 9–27. https://doi.org/10.2307/2288914

Ruppert, N. A., Rollins, C., Zhang, A., Meng, L., Holtkamp, S. G., West, M. E., & Freymueller, J. T. (2018). Complex faulting and triggered rupture during the 2018 M_W 7.9 offshore Kodiak, Alaska, earthquake. *Geophysical Research Letters*, *45*, 7533–7541. https://doi.org/10.1029/2018GL078931

Shearer, P., Hauksson, E., & Lin, G. (2005). Southern California hypocenter relocation with waveform cross-correlation, Part 2: Results using source-specific station terms and cluster analysis. *Bulletin of the Seismological Society of America*, *95*(3), 904–915. https://doi.org/10.1785/0120040168

Thatcher, W., & Hill, D. P. (1991). Fault orientations in extensional and conjugate strike-slip environments and their implications. *Geology*, *19*(11), 1116–1120. https://doi.org/10.1130/0091-7613(1991)019<1116:FOIEAC>2.3.CO;2

Wald, D. J., Heaton, T. H., & Hudnut, K. W. (1996). The slip history of the 1994 Northridge, California, earthquake determined from strong-motion, teleseismic, GPS, and leveling data. *Bulletin of the Seismological Society of America*, *86*(1B), S49–S70.

Wang, R., Schurr, B., Milkereit, C., Shao, Z., & Jin, M. (2011). An improved automatic scheme for empirical baseline correction of digital strong-motion records. *Bulletin of the Seismological Society of America*, *101*(5), 2029–2044. https://doi.org/10.1785/0120110039

Wang, T., Wei, S., Shi, X., Qiu, Q., Li, L., Peng, D., et al. (2018). The 2016 Kaikoura earthquake: Simultaneous rupture of the subduction interface and overlying faults. *Earth and Planetary Science Letters*, *482*, 44–51. https://doi.org/10.1016/j.epsl.2017.10.056

Wei, S., Helmberger, D., & Avouac, J.-P. (2013). Modeling the 2012 Wharton basin earthquakes off-Sumatra: Complete lithospheric failure. *Journal of Geophysical Research: Solid Earth*, *118*, 3592–3609. https://doi.org/10.1002/jgrb.50267

Wen, Y., Guo, Z., Xu, C., Xu, G., & Song, C. (2019). Coseismic and postseismic deformation associated with the 2018 MW 7.9 Kodiak, Alaska, earthquake from low-rate and high-rate GPS observation. *Bulletin of the Seismological Society of America*, *109*(3), 908–918. https://doi.org/10.1785/0120180246

Xie, X., & Yao, Z. (1989). A generalized reflection-transmission coefficient matrix method to calculate static displacement field of a dislocation source in a stratified half space. *Chinese Journal of Geophysics*, *32*, 191–205.

Yagi, Y., Okuwaki, R., Enescu, B., Kasahara, A., Miyakawa, A., & Otsubo, M. (2016). Rupture process of the 2016 Kumamoto earthquake in relation to the thermal structure around Aso volcano. *Earth, Planets and Space*, *68*, 118. https://doi.org/10.1186/s40623-016-0492-3

Ye, L., Lay, T., & Kanamori, H. (2015). Strike-slip faulting energy release and supershear rupture. Abstract of poster presentation, annual meeting Southern California Earthquake Center. https://www.scec.org/meetings/2015am/index.html

Ye, L., Lay, T., Kanamori, H., & Rivera, L. (2016). Rupture characteristics of major and great ($M_W \geq 7.0$) megathrust earthquakes from 1990 to 2015: 1. Source parameter scaling relationships. *Journal of Geophysical Research: Solid Earth*, *121*, 826–844. https://doi.org/10.1002/2015JB012426

Yue, H., Lay, T., & Koper, K. D. (2012). En echelon and orthogonal fault ruptures of the 11 April 2012 great intraplate earthquakes. *Nature*, *490*(7419), 245–249. https://doi.org/10.1038/nature11492

Zhao, B., Qi, Y., Wang, D., Yu, J., Li, Q., & Zhang, C. (2019). Coseismic slip model of the 2018 M_W 7.9 Gulf of Alaska earthquake and its seismic hazard implications. *Seismological Research Letters*, *90*(2A), 642–648. https://doi.org/10.1785/0220180141

Zhu, L., & Rivera, L. A. (2002). A note on the dynamic and static displacements from a point source in multilayered media. *Geophysical Journal International*, *148*(3), 619–627. https://doi.org/10.1046/j.1365-246X.2002.01610.x

Reference From Supporting Information

Wald, D. J., & Heaton, T. H. (1994). Spatial and temporal distribution of slip for the 1992 Landers, California, earthquake. *Bulletin of the Seismological Society of America*, *84*(3), 668–691.

Wells, D. L., & Coppersmith, K. J. (1994). New cc magnitude, rupture length, rupture width, rupture area and surface displacement. *Bulletin of the Seismological Society of America*, *84*(4), 9074–1002.